Letter

Bending stiffness collapse, buckling, topological bands of freestanding twisted bilayer graphene

Jin Wang [1,*] Ali Khosravi [1,2,3,*] Andrea Silva [1,3] Michele Fabrizio,[1] Andrea Vanossi [1,3] and Erio Tosatti [1,2,3,†]

[1]*International School for Advanced Studies (SISSA), Via Bonomea 265, 34136 Trieste, Italy*
[2]*International Centre for Theoretical Physics (ICTP), Strada Costiera 11, 34151 Trieste, Italy*
[3]*CNR-IOM, Consiglio Nazionale delle Ricerche - Istituto Officina dei Materiali,*
c/o SISSA, Via Bonomea 265, 34136 Trieste, Italy

The freestanding twisted bilayer graphene (TBG) is unstable, below a critical twist angle $\theta_c \sim 3.7°$, against a moiré (2×1) buckling distortion at $T = 0$. Realistic simulations reveal the concurrent unexpected collapse of the bending rigidity, an unrelated macroscopic mechanical parameter. An analytical model connects bending and buckling anomalies at $T = 0$, but as temperature rises the former fades, while buckling persists further. The (2×1) electronic properties are also surprising. The magic twist angle narrow bands, now eight in number, fail to show zone boundary splittings despite the different periodicity. Symmetry shows how this is dictated by an effective single-valley physics. These structural, critical, and electronic predictions promise to make the freestanding state of TBG especially interesting.

Two-dimensional (2D) bilayers and multilayers with variable lattice mismatch and/or twist angles exhibit a host of physical properties that also hold promise for applications [1–4]. With exceptional electronic properties at the magic twist angle, twisted bilayer graphene (TBG) is prominent among them [5–7]. Experimental bilayers are generally studied in deposited/encapsulated configurations, which preserve a flat geometry and the twist-related moiré pattern plays no mechanical role. Yet, TBG may also be realized as freestanding [8,9]. Below a critical twist angle θ_c, moiré-related structural instabilities and a variety of "buckled" states were suggested by pioneering freestanding simulations [10–12], but the actual nature and properties of the true TBG buckled state remain unknown. We use here theory and simulation to show that the moiré buckled state formed at a low twist angle is quite different from expectations. Mechanically, it is accompanied by the unanticipated collapse of the TBG macroscopic bending rigidity. Electronically, the magic twist angle narrow bands, now doubled in number, are unexpectedly degenerate at the zone boundaries, the vanishing Bragg scattering symmetry motivated reflecting single-valley physics.

Starting with molecular dynamics (MD) simulations, large-size model TBGs with variable twist θ and variable numbers N_{moire} of moiré cells were constructed with periodic boundary conditions in the (x, y) plane. Based on well-tested interatomic interactions and protocols (detailed in the Supplemental Material [13]) we sought the zero stress equilibrium $T = 0$ structure versus θ. We found that, similar but not identical to suggestions [10–12], two regimes emerge, separated by a structural phase transition at a critical $\theta_c \approx 3.77°$. Above θ_c the two layers remain flat and specular relative to the central

plane [Fig. 1(b)]. Below θ_c the layers jointly buckle, giving rise to a "moiré (2×1)" cell doubling along the armchair direction x, leading to two inequivalent, z-antisymmetrical AA nodes, AA1 (up) and AA2 (down) per cell, as in Fig. 1(a). The magnitude of buckling is large. At the magic twist angle $\theta_m \approx 1.08°$, for example, the zigzag z corrugation is ≈ 10 Å [Figs. 1(a) and 1(c)]. A competing $(\sqrt{3} \times \sqrt{3})$ buckling distortion, with one AA1 (100% up) hexagonally surrounded by AA2 and AA3 (50% down), was also found. It led to a slightly lower-energy gain, and its details are not further pursued here (see, however, Supplemental Material [13] Sec. VIII).

The energy gain driving the buckling distortion at $\theta < \theta_c$ is interlayered, with increased AB and BA, Bernal stacked areas, relative to the flat, unbuckled state's. That gain is balanced by an intralayer cost concentrated at the AA nodes, now transformed into buckling "hinges" AA1 (up) and AA2 (down). As θ decreases, the 2D density of AA nodes, thus of hinges, drops $\sim\theta^2$, and so does the cost, eventually favoring buckling for $\theta \lesssim \theta_c$. The transition, simulated by maintaining zero external stress and zero temperature, was found to be continuous. We define the $T = 0$ K buckling order parameter Q_0 as the large-size average Fourier component of the (2×1) moiré corrugation

$$Q_0 = \frac{a_{\text{Gr}}}{N_x N_y A} \left\langle \sum_{n=1}^{N_{\text{at}}} z_n \exp\left(-\frac{2\pi i}{l_x} x_n\right) \right\rangle, \quad (1)$$

where a_{Gr} is graphene's lattice constant, $l_x = \sqrt{3}\lambda$ is the size of the buckled unit cell along the armchair direction x [Figs. 1(a) and 1(b)], $\lambda \sim a_{\text{Gr}}/\theta$ is the moiré lattice constant [Figs. 1(a) and 1(b)], x_n and z_n are coordinates of the nth atom $(n = 1, 2, \ldots, N_{\text{at}})$, $A = \sqrt{3}\lambda^2$ is the buckled unit cell area, and N_x, N_y are the number of cell replicas along x and y. This $Q_0(\theta)$ is proportional to the buckling-induced bilayer thickness increase $\langle (z_{AA1} - z_{AA2}) \rangle$ [inset of Fig. 1(c)]. Simulation

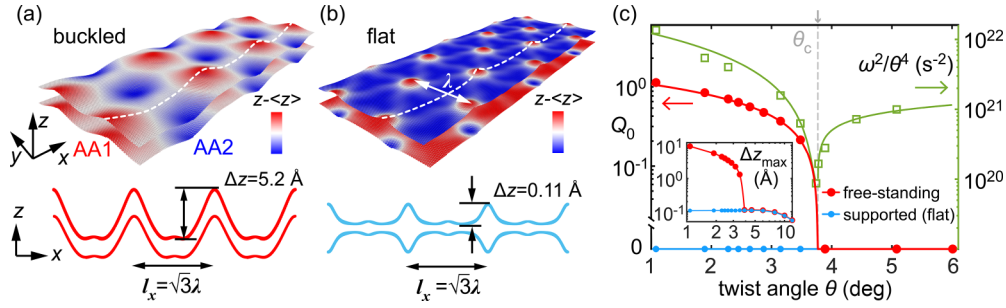*These authors contributed equally to this work.
†tosatti@sissa.it

FIG. 1. Visual models of small twist angle TBG structure at $T = 0$. Out-of-plane displacements of (a) optimal freestanding (2×1) buckled and (b) flat structures, magnified by factors 3 and 100, respectively, are sketched for twist angle $\theta_m = 1.08°$, where the moiré size $\lambda \approx a_{Gr}/\theta_m \approx 13$ nm. (c) Twist angle dependence of the optimal buckling order parameter Q_0 (red and blue, left axis) for $N_x = N_y = 1$, $T = 0$ K, and of the normalized soft phonon frequencies ω^2/θ^4 (right axis, green). Critical twist angle $\theta_c \approx 3.77°$ marked by a gray dashed line. Red and green lines are power-law fits as described in text. The inset shows the maximum out-of-plane corrugation Δz_{max}.

for a set of θ values (see Supplemental Material [13] Sec. I) characterized by a sufficient numbers of moiré cells N_{moire} showed, at $T = 0$, a growth of $Q_0(\theta < \theta_c)$ [Fig. 1(c)] well approximated by a power-law rise $Q_0(\theta) \approx 0.48\Theta(\theta_c - \theta)(\theta_c - \theta)^\beta$, where Θ is the Heaviside function, and $\beta = 0.7(0)$ a critical exponent. Within fitting uncertainty, reflected by the second decimal in parentheses, this exponent differs from $1/2$, which could be expected for a classical $T = 0$ transition.

As in other displacive phase transitions, the local free energy around equilibrium supports a soft buckling phonon mode ω_i [$i = (+, -)$ refers to above or below θ_c], a mode which will also control critical fluctuations at $T > 0$. Its frequency was extracted from oscillations around equilibrium of a (2×1) moiré cell by starting the dynamics with $Q = Q_0 + \delta Q$, with $|\delta Q|/Q_0 \ll 1$, while maintaining $T = 0$ and zero stress. Because the cell area $A(\theta)$ varies as θ^{-2}, it is convenient to further normalize the soft mode frequencies to constant area in the form ω^2/θ^4. Power-law fits near the singularity at θ_c yield [Fig. 1(c)], $\omega_i^2/\theta^4 \sim a_i|\theta - \theta_c|^{\gamma_i}$, with $\gamma_+ = 0.3(7)$, $\gamma_- = 1.3(0)$, with $a_+ = 8.58 \times 10^{20}$ s^{-2}, $a_- = 3.24 \times 10^{21}$ s^{-2}. Note the strongly asymmetric, again unusual exponents. We observe nevertheless that $\gamma_-/\beta \approx 2$ as in standard mean-field theory.

More interestingly, the buckling amplitude Q_0 and its soft mode frequency are not the only critical quantities at $\theta \to \theta_c$. We found an unexpected macroscopic partner, the bilayer's bending stiffness. Defined for direction $\mu = (x, y)$ as $D_\mu = dF/d[(\partial^2 h/\partial\mu^2)^2]$, where F is the Helmholtz free-energy density, $\partial^2 h/\partial\mu^2$ is the μth component of the 2D Laplacian, and h the bilayer's corrugation profile $h(x, y)$ (Fig. 2). Controlling the membrane's deviations from planarity, D_μ determines the macroscopic flexural mode dispersion along μ, $\omega_\mu(q_\mu) = (D_\mu/\rho_{2D})^{1/2}q_\mu^2$, of an infinite membrane of 2D density ρ_{2D}.

The freestanding TBG bending stiffness D_μ was extracted by starting simulations with a slight x compression (Fig. 2), i.e., $L_\mu = L_{0\mu} - \delta L$, of the bilayer's zero-pressure equilibrium size. Either the initial energy increase δE, or the ensuing flexural oscillation ω_μ yield $D_\mu = \lim_{\delta E \to 0} \frac{L_\mu^4 \delta E}{\pi^4 A h^2} = \frac{\rho_{2D} L_\mu^4 \omega_\mu^2}{16\pi^4}$ [14]. The resulting D_x is shown in Fig. 2. For $6° < \theta < 30°$, D_x is close to $2D_0$, where $D_0 = 1.44$ eV is the bending stiffness of monolayer graphene [15], the factor 2 reflecting free sliding

between the two layers [16,17]. At the opposite end $\theta = 0°$, layers are instead locked in Bernal's AB stacking. That pushes D_x up to $D_B \approx 100$ eV, now reflecting the large in-plane stiffness of graphene [18,19]. Between these extremes, D_x drops below $2D_0$ when $\theta \lesssim 6°$, critically collapsing at θ_c, and rising immediately below towards D_B. Near θ_c the collapse is critical,

$$D_x(\theta) \sim c_i|\theta - \theta_c|^{\epsilon_i}, \qquad (2)$$

with exponents $\epsilon_+ = 0.2(2)$ and $\epsilon_- = 1.4(4)$, and $c_+ = 2.4$ eV and $c_- = 7.5$ eV, for $\theta > \theta_c$ and $\theta < \theta_c$, respectively.

Why does a *macroscopic* mechanical parameter such as $D_x(\theta)$ drop critically at the *microscopic* buckling transition? We developed an analytical "zigzag" model that explains it. As sketched in Fig. 3(a) the buckled structure can roughly be modeled as a zigzag shape where flat (AB-commensurate) regions are separated by maximally bent (AA-centered) hinges. The total length of the system along the buckling direction is $L_x = N_x l_x$. Upon bending along x both hinges and flats undergo deformation, and the free-energy increase with bending angle Φ is $F(\Phi) = \frac{D_f K l_y}{2N(2D_f l_y + K l_x)}\Phi^2$ where D_f is the bending
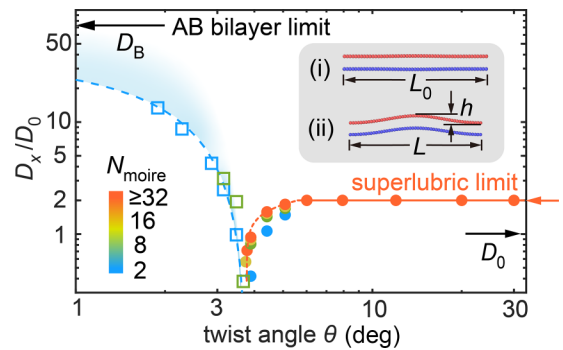

FIG. 2. Freestanding TBG bending stiffness D_x/D_0, normalized to the monolayer's D_0, from zero stress simulations at $T = 0$. Note the critical collapse (red circles for $\theta > \theta_c$, blue squares for $\theta < \theta_c$). Dashed and dotted curves are power-law fits near θ_c. Multiplicity of circles at the same twist angle shows convergence for simulation cells with increasing size N_{moire} (the N_{moire} dependence is weak for $\theta < \theta_c$). Inset: Simulation protocol (see text).
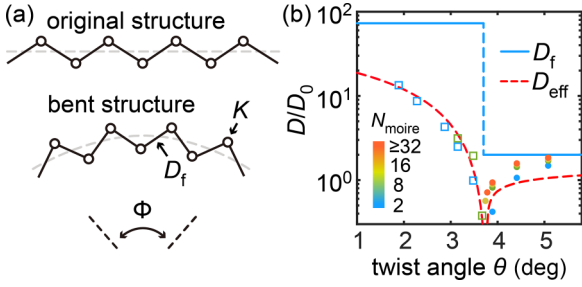
FIG. 3. Zigzag model of bending stiffness D_{eff} in a buckled bilayer. (a) Unbent and bent models; (b) bending stiffness from real simulations of Fig. 2 (circles and squares) and from the zizgag model, Eq. (3) (red dashed line). Assumed flat piece stiffness D_f (blue line) (more detail in Supplemental Material [13] Sec. V).

stiffness of the flat pieces, K the angular stiffness of the hinges, and l_y the bilayer size perpendicular to the bending direction x. Defining an effective bending stiffness $F = \frac{D_{eff} l_y}{2L_x} \Phi^2$, one obtains, using $l_y = \lambda$,

$$D_{eff} = \frac{D_f}{1 + 2D_f/\sqrt{3}K}. \tag{3}$$

We can now assume $D_f = D_B \approx 100$ eV of the flat pieces for $\theta < \theta_c$, dropping to $D_f = 2D_0 = 2.88$ eV for $\theta > \theta_c$ [Fig. 3(b)]. The collapse of $D_x(\theta)$ at θ_c is controlled by that of the hinge stiffness K, connected to the buckling frequency $\omega_\pm$ by simple mechanics

$$K \propto \rho_{2D} l_x^4 \omega_\pm^2. \tag{4}$$

Inserting $\omega_\pm$ into Fig. 3(b), theoretical and simulated bending stiffnesses agree fairly well, both in magnitude and in critical scaling (details in Supplemental Material [13] Sec. V). Thus the TBG bending stiffness collapse is a direct consequence of that of the buckling modes $\omega_\pm$. In return, the buckling criticality must be influenced by the bending one. The coexistence of these two coupled degrees of freedom, with important cross correlations, is likely to account for the unusual exponents.

We come next to two important properties predicted for the freestanding TBG buckled state, namely temperature behavior, and the narrow-band electronic structure at the magic twist angles.

Temperature. Finite-temperature MD simulations show that at a small twist angle the buckling persists up to high temperature. Flexural fluctuations, abundant and not gapped, do not cancel the buckling order parameter, which survives up to a remarkable ≈ 500 K at the magic twist angle [Fig. 4(a)]. If bending could be ignored, this robust buckling order should drop at some T_c with three-state Potts universality, whose behavior is critical as opposed to first order, despite the presence of Landau third-order invariants [20,21]. Unfortunately, size limitations obscure the precise high-temperature buckling demise, replacing it with the smooth crossovers of Fig. 4(a) (see Supplemental Material [13] Sec. IV), equally compatible with either continuous or discontinuous decays. We also extracted the temperature dependence of bending stiffness [Fig. 4(b)]. We do not deal with the long-wavelength anomaly of the freestanding bilayer as a membrane [22], but simply extract the buckling-related evolution, as predicted
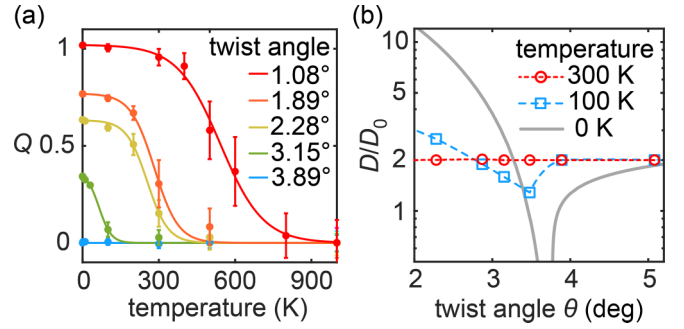

FIG. 4. Effect of temperature. (a) Buckling order parameter at high temperatures. The expected critical behavior is smoothened by a small simulation size [three (2×1) cells at each θ]. (b) Bending stiffness at $T = 0$ (gray, from Fig. 2), 100 K (blue), and 300 K (red). Note the extreme sensitivity to temperature.

for observation in microscopic size samples. Contrary to the buckling robustness, bending stiffness changes dramatically with temperature. The singularity near θ_c is quickly wiped out [Fig. 4(b)], the two layers eventually bending independently despite the large buckling. Reflecting that, the flexural fluctuations of a TBG near θ_c should grow anomalously at low temperature, when D_x is small, but not above.

Electronic structure. Near the magic twist angle $\theta_m = 1.08°$, the flat TBG has four ultranarrow bands, whose physics has been at the center of much attention [5,6]. What will happen of these bands in the freestanding TBG, where the buckling sets in? We should anticipate eight narrow bands, separated by zone boundary gaps caused by the large (2×1) distortion. We carried out tight-binding calculations at θ_m and compared buckled and unbuckled TBG. Shown in Fig. 5 [23] are the eight bands of the buckled state. The bands, almost a factor 2 wider, display the following: First, unlike the unbuckled TBG [or even the nonoptimal (1×1) buckled state [12]] the Dirac zero gap, formerly at point K, is now split into two close-by points $K \pm k_y$ (see the inset). Second, and striking, zone boundary splittings at the W and X points—expected because (2×1) buckling removes the C_{3z} symmetry, and Bragg scattering should in principle take place—do not occur. This anomaly calls for a full symmetry analysis.

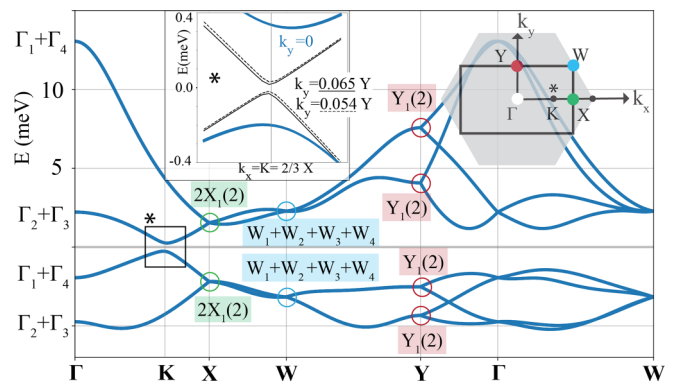FIG. 5. The eight narrow bands of the (2×1) buckled TBG at the twist angle $\theta = 1.08°$ (see Ref. [23]). Inset * shows how the gap closing point is now split into two, above and below (not shown) the point K where it lies in the flat TBG.

The buckled structure has, unlike the flat one, a nonsymmorphic space group $P2_12_12$ (No. 18) that includes $\{1 \mid 0\}$, $\{2_{010} \mid 0, 1/2, 0\}$, $\{2_{100} \mid 1/2, 0, 0\}$, and $\{2_{001} \mid 1/2, 1/2, 0\}$, (in Seitz notation, with fractional translations) which we shortly denote as E, C_{2y}, C_{2x}, and C_{2z}, respectively. The Bloch states of the eight bands at the high-symmetry points transform as the irreducible representations (irreps) of the corresponding little groups (see Table S3 in the Supplemental Material [13]). In our reference frame only C_{2y} commutes with the generator of $U(1)$ valley symmetry, while C_{2x}, and thus C_{2z}, exchange the valley index—as time-reversal symmetry $\hat{T}$ also does. It follows that, e.g., at the Γ point, C_{2x} and valley $U(1)$ get promoted to $SU(2)$. That enforces degeneracy between eigenstates with opposite parity under C_{2x} and the same parity under C_{2y} [24], making Γ_1 degenerate with Γ_4, and Γ_2 with Γ_3. The interplay between valley $U(1)$ and the nonsymmorphic group's fractional translations has further consequences at the zone boundary points **W** and **X**. Physical insight is obtained by switching to a single-valley representation where the valley index is conserved [25]. This representation obeys the magnetic space group $P2_12_1'2'$ (No. 18.19) generated by E, C_{2y}, $\hat{T}C_{2x}$, and $\hat{T}C_{2z}$. The four flat bands per valley can be generated by Wannier orbitals centered at the Bernal stacked regions. Their centers correspond to the Wyckoff positions $4c$ in the magnetic space group $P2_12_1'2'$ [26], whose corepresentation contains just the identity and thus allows a single irrep. The single-valley elementary band representation is [26] $2\Gamma_1(+) \oplus 2\Gamma_2(-)$ and $2Y_1(+) \oplus 2Y_2(-)$, where $(\pm)$ indicate the parity under C_{2y}; $X_1X_2(2)$ and $W_1W_2(2)$, transforming under C_{2y}, respectively, as σ_3, the third Pauli matrix, and $i\sigma_3$ (see Table S3). Along the path $\mathbf{X} \to \mathbf{W}$, $k_y \in 0 \to \pi$, the irreducible representation remains twofold degenerate and transforms under C_{2y} as $e^{ik_y/2}\sigma_3$. This now yields double degeneracies within a single valley. Bearing in mind that the two valleys must be further degenerate at all high-symmetry points and paths that are invariant under C_{2x}, one readily recovers the fourfold degeneracy at **W**. In fact, all "accidental" degeneracies of the band structure in Fig. 5 are explained in terms of single-valley physics, enforced by nonsymmorphicity.

These one-electron degeneracies, and the ways they might be broken by interactions, represent an interesting question for freestanding TBG experiments, where topology should also play a role. Since narrow bands do admit an elementary representation, the arguments used in the unbuckled case to diagnose a fragile topology [25] do not strictly apply here. The unexpected similarity of buckled bands to the (2×1) Brillouin zone (BZ) folded unbuckled ones (Fig. S12) nonetheless suggests that the topological properties remain similar. Thus [24,27] the interplay between Coulomb repulsion and electron-phonon coupling to Kekulé modes should split the degeneracies and open the gaps that are absent at the one-electron level, stabilizing topological insulators in (2×1) buckled TBG, giving rise to fractional fillings absent in the flat state (see Supplemental Material [13] Sec. VI).

In summary, several important phenomena are predicted to occur once freestanding TBG will be realized. First, a zigzag buckled state should set in with a critical behavior as a function of twist angle $\theta \to \theta_c \approx 3.7°$. At $\theta \approx 1°$ the normals to the bilayer should deviate from $\hat{z}$ by a sizable $\sim \pm 3°$ (Supplemental Material [13] Sec. VII), experimentally observable. Second, the macroscopic bending stiffness, a crucial mechanical parameter for a membrane, should collapse at the buckling transition, giving rise to gigantic flexural fluctuations already at very low temperatures. Third, the buckling distortion should survive up to relatively high temperatures, whereas the bending stiffness anomaly will on the contrary dwindle upon heating. Fourth, narrow electronic bands are predicted for the buckled magic TBG displaying unexpected single-valley degeneracies, to be broken by interactions, with the possibility of doubling the number of quantized fillings upon gating. That should offer a richer playground for topological features and insulating states than for flat TBG. Other properties including kinetic and tribological behavior will be addressed in follow-up work. Similar buckling phenomena could take place in freestanding bilayers of other 2D materials, now being pursued.

[1] A. K. Geim and I. V. Grigorieva, Nature (London) **499**, 419 (2013).

[2] K. S. Novoselov, A. Mishchenko, A. Carvalho, and A. H. Castro Neto, Science **353**, aac9439 (2016).

[3] M. Yankowitz, Q. Ma, P. Jarillo-Herrero, and B. J. LeRoy, Nat. Rev. Phys. **1**, 112 (2019).

[4] Y. Liu, N. O. Weiss, X. Duan, H. C. Cheng, Y. Huang, and X. Duan, Nat. Rev. Mater. **1**, 16042 (2016).

[5] R. Bistritzer and A. H. MacDonald, Proc. Natl. Acad. Sci. USA **108**, 12233 (2011).

[6] Y. Cao, V. Fatemi, A. Demir, S. Fang, S. L. Tomarken, J. Y. Luo, J. D. Sanchez-Yamagishi, K. Watanabe, T. Taniguchi, E. Kaxiras, R. C. Ashoori, and P. Jarillo-Herrero, Nature (London) **556**, 80 (2018).

[7] Y. Cao, V. Fatemi, S. Fang, K. Watanabe, T. Taniguchi, E. Kaxiras, and P. Jarillo-Herrero, Nature (London) **556**, 43 (2018).

[8] B. Butz, C. Dolle, F. Niekiel, K. Weber, D. Waldmann, H. B. Weber, B. Meyer, and E. Spiecker, Nature (London) **505**, 533 (2014).

[9] Y. Ying, Z. Z. Zhang, J. Moser, Z. J. Su, X. X. Song, and G. P. Guo, Nat. Commun. **13**, 6392 (2022).

[10] S. Dai, Y. Xiang, and D. J. Srolovitz, Nano Lett. **16**, 5923 (2016).

[11] M. Lamparski, B. Van Troeye, and V. Meunier, 2D Mater. **7**, 025050 (2020).

[12] T. Rakib, P. Pochet, E. Ertekin, and H. T. Johnson, Commun. Phys. **5**, 242 (2022).

[13] See Supplemental Material at http://link.aps.org/supplemental/ 10.1103/PhysRevB.108.L081407 for simulation details, definition of the buckling order parameter, details on the zigzag model, finite-temperature effects, tilt angle, $\sqrt{3} \times \sqrt{3}$ buckling, details on the tight-binding calculation, and the limiting behavior near zero twist, which includes Refs. [16,17,24,25,28–38].

[14] L. D. Landau, E. M. Lifshitz, A. M. Kosevich, and L. P. Pitaevskii, *Theory of Elasticity*, Vol. 7 (Elsevier, Amsterdam, 1986).

[15] Q. Lu, M. Arroyo, and R. Huang, J. Phys. D: Appl. Phys. **42**, 102002 (2009).

[16] E. Han, J. Yu, E. Annevelink, J. Son, D. A. Kang, K. Watanabe, T. Taniguchi, E. Ertekin, P. Y. Huang, and A. M. van der Zande, Nat. Mater. **19**, 305 (2020).

[17] J. Yu, E. Han, M. A. Hossain, K. Watanabe, T. Taniguchi, E. Ertekin, A. M. van der Zande, and P. Y. Huang, Adv. Mater. **33**, 2007269 (2021).

[18] J. U. Lee, D. Yoon, and H. Cheong, Nano Lett. **12**, 4444 (2012).

[19] G. Wang, Z. Dai, J. Xiao, S. Z. Feng, C. Weng, L. Liu, Z. Xu, R. Huang, and Z. Zhang, Phys. Rev. Lett. **123**, 116101 (2019).

[20] F. Y. Wu, Rev. Mod. Phys. **54**, 235 (1982).

[21] Under uniaxial stress or an asymmetric boundary condition, such as sketched in Figs. 1(a) and 1(b), that behavior might turn to Ising.

[22] D. R. Nelson and L. Peliti, J. Phys. France **48**, 1085 (1987).

[23] In order to be consistent with conventions of Ref. [6], the *x* and *y* directions in the electronic section are exchanged with respect to the structural part.

[24] M. Angeli, E. Tosatti, and M. Fabrizio, Phys. Rev. X **9**, 041010 (2019).

[25] Z. Song, Z. Wang, W. Shi, G. Li, C. Fang, and B. A. Bernevig, Phys. Rev. Lett. **123**, 036401 (2019).

[26] M. I. Aroyo, J. M. Perez-Mato, D. Orobengoa, E. Tasci, G. de la Flor, and A. Kirov, Bulg. Chem. Commun. **43**, 183 (2011); M. I. Aroyo, J. M. Perez-Mato, C. Capillas, E. Kroumova, S. Ivantchev, G. Madariaga, A. Kirov, and H. Wondratschek, Z. Kristallogr. Cryst. Mater. **221**, 15 (2006); M. I. Aroyo, A. Kirov, C. Capillas, J. M. Perez-Mato, and H. Wondratschek, Acta Crystallogr. A **62**, 115 (2006).

[27] A. Blason and M. Fabrizio, Phys. Rev. B **106**, 235112 (2022).

[28] G. Trambly de Laissardière, D. Mayou, and L. Magaud, Nano Lett. **10**, 804 (2010).

[29] A. N. Kolmogorov and V. H. Crespi, Phys. Rev. B **71**, 235415 (2005).

[30] W. Ouyang, D. Mandelli, M. Urbakh, and O. Hod, Nano Lett. **18**, 6009 (2018).

[31] D. W. Brenner, O. A. Shenderova, J. A. Harrison, S. J. Stuart, B. Ni, and S. B. Sinnott, J. Phys.: Condens. Matter **14**, 783 (2002).

[32] S. Plimpton, J. Comput. Phys. **117**, 1 (1995).

[33] A. P. Thompson, H. M. Aktulga, R. Berger, D. S. Bolintineanu, W. M. Brown, P. S. Crozier, P. J. in 't Veld, A. Kohlmeyer, S. G. Moore, T. D. Nguyen, R. Shan, M. J. Stevens, J. Tranchida, C. Trott, and S. J. Plimpton, Comput. Phys. Commun. **271**, 108171 (2022).

[34] E. Bitzek, P. Koskinen, F. Gähler, M. Moseler, and P. Gumbsch, Phys. Rev. Lett. **97**, 170201 (2006).

[35] G. J. Martyna, D. J. Tobias, and M. L. Klein, J. Chem. Phys. **101**, 4177 (1994).

[36] A. Fasolino, J. H. Los, and M. I. Katsnelson, Nat. Mater. **6**, 858 (2007).

[37] J. A. Thomas, J. E. Turney, R. M. Iutzi, C. H. Amon, and A. J. H. McGaughey, Phys. Rev. B **81**, 081411(R) (2010).

[38] J. C. Slater and G. F. Koster, Phys. Rev. **94**, 1498 (1954).